

1 ***This Looks Like That There: Interpretable neural networks for image tasks***
2 **when location matters**

3 Elizabeth A. Barnes,^a Randal J. Barnes,^b Zane K. Martin,^a and Jamin K. Rader,^a

4 ^a*Department of Atmospheric Science, Colorado State University, Fort Collins, CO, USA.*

5 ^b*Civil, Environmental, and Geo- Engineering, University of Minnesota, Minneapolis, MN, USA.*

6 *Corresponding author:* Elizabeth A. Barnes, eabarnes@colostate.edu

7 ABSTRACT: We develop and demonstrate a new interpretable deep learning model specifically
8 designed for image analysis in earth system science applications. The neural network is designed to
9 be inherently interpretable, rather than explained via *post hoc* methods. This is achieved by training
10 the network to identify parts of training images that act as prototypes for correctly classifying
11 unseen images. The new network architecture extends the interpretable prototype architecture of a
12 previous study in computer science to incorporate absolute location. This is useful for earth system
13 science where images are typically the result of physics-based processes, and the information is
14 often geo-located. Although the network is constrained to only learn via similarities to a small
15 number of learned prototypes, it can be trained to exhibit only a minimal reduction in accuracy
16 compared to non-interpretable architectures. We apply the new model to two earth science use
17 cases: a synthetic data set that loosely represents atmospheric high- and low-pressure systems, and
18 atmospheric reanalysis fields to identify the state of tropical convective activity associated with the
19 Madden-Julian oscillation. In both cases, we demonstrate that considering absolute location greatly
20 improves testing accuracies. Furthermore, the network architecture identifies specific historical
21 dates that capture multivariate, prototypical behaviour of tropical climate variability.

22 SIGNIFICANCE STATEMENT: Machine learning models are incredibly powerful predictors,
23 but are often opaque “black boxes”. The how-and-why the model makes its predictions is inscrutable
24 — the model is not interpretable. We introduce a new machine learning model specifically designed
25 for image analysis in earth system science applications. The model is designed to be inherently
26 interpretable and extends previous work in computer science to incorporate location information.
27 This is important because images in earth system science are typically the result of physics-based
28 processes, and the information is often map based. We demonstrate its use for two earth science use
29 cases and show that the interpretable network exhibits only a small reduction in accuracy compared
30 to black box models.

31 1. Introduction

32 Machine learning has been identified as an innovative, under-explored tool for furthering under-
33 standing and simulation of the Earth system (Balmaseda et al. 2020; Irrgang et al. 2021; National
34 Academies of Sciences Engineering and Medicine 2020). Artificial neural networks (a type of su-
35 pervised machine learning) have emerged as a powerful tool for extracting nonlinear relationships
36 amidst noisy data, and thus are particularly suited to this endeavor. However, a major criticism of
37 the use of neural network models for scientific applications is that they are “black boxes.” Scientists
38 typically want to know why the model reached the decision that it did. The benefit of explaining
39 the decision-making process of a model goes beyond that of satisfying curiosity: explanation can
40 assist users in (1) determining if the model is getting the right answers for the right reasons (e.g.
41 Lapuschkin et al. 2019), (2) controlling and improving the machine learning approach (e.g. Keys
42 et al. 2021), and (3) discovering new science (e.g. Toms et al. 2020; Barnes et al. 2020).

43 Because researchers are driven by the desire to explain the decision-making process of deep
44 learning models, a large variety of *post hoc* explainability methods have been developed (e.g.
45 Buhrmester et al. 2019; Barredo Arrieta et al. 2020; Samek et al. 2021). By *post hoc*, we mean
46 methods in which a deep learning model has already been trained and the user attempts to explain
47 the predictions of the black box model after the predictions have been made. Although *post hoc*
48 explainability methods have demonstrated success across many scientific applications (including
49 earth system science, e.g. McGovern et al. (2019); Toms et al. (2020); Davenport and Diffenbaugh
50 (2021)), they are not without their drawbacks. *Post hoc* explainability methods do not exactly

51 replicate the computations made by the black box model. Instead, through a set of assumptions and
52 simplifications, these methods quantify some reduced version of the model (e.g. Montavon et al.
53 2018) and, thus, do not explain the actual decision-making process of the network. Furthermore,
54 the explanations are not always reliable (Kindermans et al. 2019). Different explanation methods
55 can produce vastly different explanations of the exact same black box model (Mamalakos et al.
56 2021). Even if the explanation is reliable, at times the output of the explainability method itself
57 requires extensive deciphering by the scientist to understand the result. Rudin (2019) discusses in
58 detail many of these potential issues with explainable machine learning methods and suggests that
59 we should instead be using machine learning models that are inherently “interpretable”. That is,
60 instead of trying to explain black box models, we should be creating models where the decision-
61 making process is interpretable by design.

62 Chen et al. (2019) present an example of one type of interpretable neural network, the *prototypical*
63 *part network* (ProtoPNet). The ProtoPNet hinges on training a neural network to identify patches
64 of the training images that act as “prototypes” for correctly classifying unseen images. The idea
65 for the ProtoPNet stems from the need to define a form of interpretability that works the way a
66 scientist might describe their way of thinking. In their specific application, Chen et al. (2019)
67 focus on classifying images of birds by their species. A scientist may classify a new bird image
68 by comparing it to representative examples of each species (i.e. species prototypes) and choosing
69 the prototype that most resembles the image, i.e. *this looks like that*. In this way, the network is
70 inherently interpretable in that the *actual* decision-making process can be linked to specific features
71 of the bird in the input image and their similarity to a relatively small number of species-specific
72 prototypes that are directly drawn from the training set. For bird species identification, Chen et al.
73 (2019) demonstrate that the ProtoPNet learns prototypes that represent distinguishing features such
74 as the red head of a red-bellied woodpecker, or the bright blue wing of a Florida jay.

75 Images in earth system science are typically the result of physics-based processes, and the
76 information is often geo-located. Thus, unlike the ProtoPNet of Chen et al. (2019) which does not
77 care *where* the bird’s wing is in the image, the location of specific earth system features can be
78 critical to the final task (although this is certainly not always the case, e.g. identification of cloud
79 types from satellite imagery; Rasp et al. (2019)). For example, the mere presence of a low-pressure
80 system on a weather map is not enough to know where it will rain. Instead, the location of the low

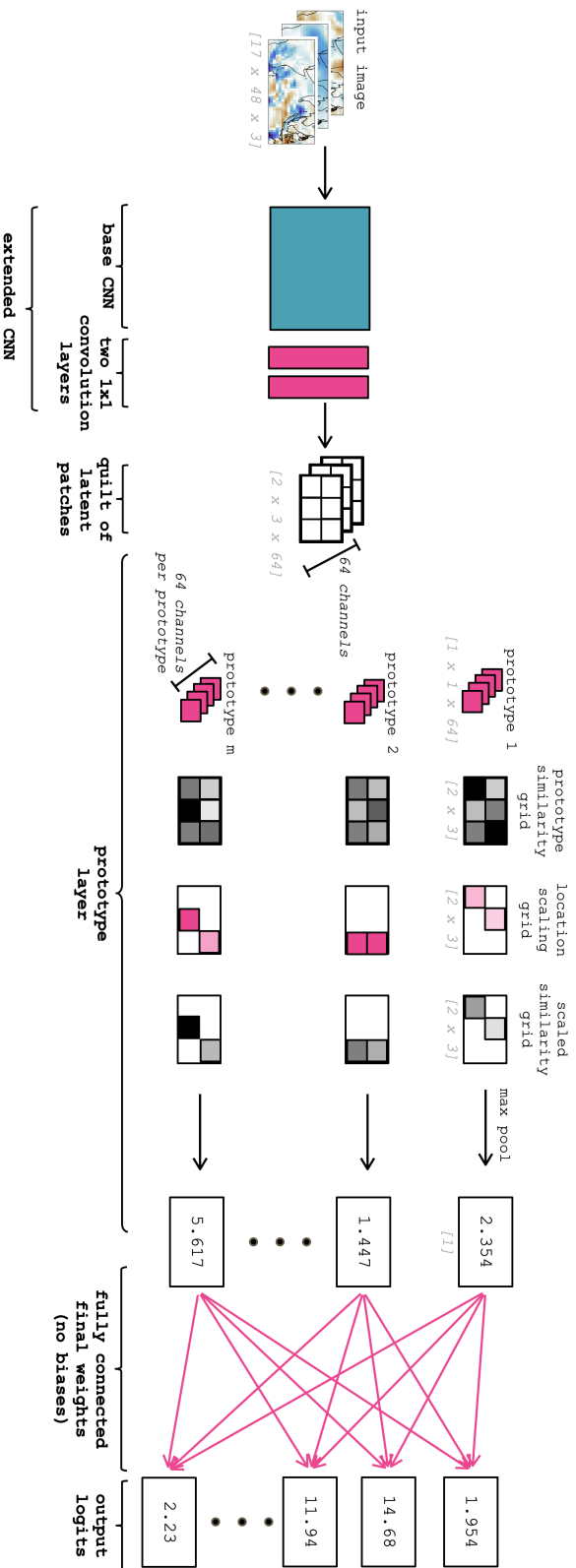
81 — *where* it is — is also vital for this task. Similarly, identifying the presence of a strong El Niño
82 requires not only warm sea-surface temperatures, but specifically warm sea-surface temperatures
83 in the tropical equatorial east Pacific (e.g. Philander 1983). Here, we extend the ProtoPNet of Chen
84 et al. (2019) to consider absolute location in the interpretable prototype architecture, which we
85 call the ProtoLNet (“Prototypical Location Network”). We demonstrate that considering absolute
86 location greatly improves the network accuracy (ProtoLNet rather than ProtoPNet) for two earth
87 science use cases. The first use case, the idealized quadrants use case (Section 3), applies the
88 ProtoLNet to a synthetic data set that loosely represents high- and low-pressure systems where the
89 need for location information is readily apparent. The second use case applies the ProtoLNet to
90 over 100 years of atmospheric reanalysis fields to identify the state of tropical convective activity
91 associated with the Madden-Julian oscillation (MJO; Madden and Julian 1971, 1972; Zhang 2005).
92 The MJO use case (Section 4) provides a real, geophysical example of how the ProtoLNet relies
93 on location information to make its predictions and demonstrates how the learned prototypes can
94 be viewed as prototypical behaviour of transient climate phenomena.

95 **2. Network Design & Training**

96 As discussed in the introduction, the ProtoLNet is largely based on the ProtoPNet of Chen et al.
97 (2019). We describe the network architecture below, highlighting where our ProtoLNet diverges
98 from the ProtoPNet of Chen et al. (2019). We then describe the training procedure in detail.

99 *a. ProtoLNet architecture*

100 The ProtoLNet is designed to classify images by comparing latent patches of the input image
101 to prototypical latent patches learned from the training set, all while explicitly considering the
102 location within the image of the similar latent patches. Throughout, we use the word “patch”
103 to refer to a group of neighboring pixels within the input image, and “latent patch” to refer to a
104 latent representation of a patch that is computed via a series of convolutional and pooling layers
105 within the convolutional neural network. In this section, we first provide a general overview of
106 the ProtoLNet architecture from start to finish, and then go into more detail about each step in
107 subsequent paragraphs, ending with the training process.



108 Fig. 1. Schematic depicting the ProtoNet architecture. Example and internally consistent dimensions of the tensors at each step are given in grey
 109 brackets, although the specific dimensions vary for each use case. Pink colors denote components of the network that are trained (learned), while gray
 110 and black colors denote components that are directly computed. The weights within the base CNN (blue shading) can either be trained or frozen.

111 The ProtoLNet architecture (Fig. 1) is very similar to that of the ProtoPNet, and starts with a
112 base convolutional neural network (CNN) chosen by the user. As discussed more in Section c, this
113 base CNN may be a pre-trained network, or a newly initialized network with randomized weights.
114 The CNN is followed by two 1×1 convolutional layers that act to restructure the dimensions of
115 the CNN output to be consistent with the subsequent prototype layer. It is within the prototype
116 layer that the interpretable learning is done. The network is trained to learn representative latent
117 patches within the training set specific to each class, termed *prototypes*, which provide evidence for
118 the image belonging to a particular class. That is, when the input image has a patch whose latent
119 representation *looks like that* prototype, it is labeled as belonging to the prototype’s associated
120 class. This is done by computing the similarity of each prototype to the latent patches of the input
121 image. Unique to our ProtoLNet, these similarity scores are scaled by a learned, prototype-specific
122 location scaling grid so that similarities to the prototypes are only important for certain locations
123 within the input image. The maximum scaled similarity score across the latent patches for each
124 prototype is then computed. These scores are connected to the output via a fully connected layer,
125 and the weighted scores are summed for each output class to produce a total number of “points”
126 for each class. The class with the highest number of points is then identified as the predicted class.

127 As will be discussed in detail in Section c, the ProtoLNet learns the convolutional kernels within
128 the two 1×1 convolution layers, the prototypes, the location scaling grid, and the final fully
129 connected weights (pink components in Fig. 1). The user must specify the number of prototypes
130 specific to each output class. For the use cases presented here, we choose an equal number of
131 prototypes for each class, so if there are n classes and p prototypes per class, then there are $m = n * p$
132 total prototypes. A critical aspect of the architecture is that *each prototype is assigned to only one*
133 *class* since it is used as evidence that a particular sample belongs its class.

134 Each sample is pushed through the extended CNN, which results in an output “quilt” of latent
135 patches. To introduce some general notation, the quilt has shape $a \times b \times D$, where $a \times b$ is the
136 new image shape after undergoing pooling in the base CNN, and D corresponds to the number of
137 convolutional kernels chosen by the user. Each prototype vector (\mathbf{p}) then has shape $1 \times 1 \times D$. To
138 simplify our discussion, from here forward we will drop the general notation and instead use the
139 specific dimensions (denoted in gray) of the example shown in Fig. 1. That is, $a = 2$, $b = 3$, and
140 $D = 64$.

141 For the example in Fig. 1, a latent patch has shape $1 \times 1 \times 64$, and the quilt of latent patches
 142 output by the extended CNN has shape $2 \times 3 \times 64$. Because the input image has already potentially
 143 undergone multiple convolutional and pooling layers within the extended CNN, these latent patches
 144 *do not* represent a single pixel of the input image, but instead are a latent representation of some
 145 larger patch within the input image. Similar to the latent patches, each of the m learned prototypes
 146 are a latent representation of some larger region of the input image. Each prototype has the same
 147 shape as a latent patch: $1 \times 1 \times 64$. The similarity score for a prototype \mathbf{p} and a latent patch \mathbf{z}
 148 is computed as a function of the distance between these two vectors (i.e. the L_2 norm of the
 149 difference). The greater the distance between, the lower the similarity score. Following Chen et al.
 150 (2019), we compute

$$151 \text{SimilarityScore} = \log\left(\frac{\|\mathbf{z} - \mathbf{p}\|_2^2 + 1}{\|\mathbf{z} - \mathbf{p}\|_2^2 + \epsilon}\right) \approx \log\left(1 + \frac{1}{(\text{distance})^2}\right) \quad (1)$$

152 where $\|\cdot\|_2^2$ is the squared L_2 norm and ϵ is a small number, there to guard against divide-by-zero
 153 problems. Applying this similarity metric to a quilt of latent patches results in $m \ 2 \times 3$ similarity
 154 grids, one for each prototype. The values within these grids thus quantify how much that latent
 155 patch of the input *looks like* each prototype.

156 In the original ProtoPNet, at this point the maximum similarity within each similarity grid is
 157 computed for each prototype. However, unique to our ProtoLNet — and indeed the novelty of
 158 this work — is that we scale each prototype’s similarity grid by a location-specific value learned
 159 by the network. This step rescales the similarities such that similarities in certain locations are
 160 accentuated and similarities in other locations are muted. To follow this paper’s title, it isn’t enough
 161 for *this* latent patch (at any location) to look like *that* prototype. Instead, *this* latent patch must look
 162 like *that* prototype in only specific locations — *there*. This results in m location-scaled similarity
 163 grids, one for each prototype.

164 Once again following the architecture of the original ProtoPNet, we apply max pooling to each
 165 scaled similarity grid to obtain a single score for the maximum similarity (scaled by the location
 166 scaling) between a prototype and the input image. These scores are then connected to the output
 167 layer via a fully connected layer with learned weights but zero bias. The choice of zero bias in the
 168 final fully-connected layer is essential for interpreting the prototypes as providing evidence for a

169 particular class. With a zero bias, the final points contributing to each class are comprised only of
170 a sum of location-scaled similarity scores multiplied by a final weight. The final weights layer is
171 trained separately from the rest of the network. The layer is trained in such a way as to keep weights
172 connecting prototypes with their associated class large, while minimizing the weights connecting
173 prototypes with their non-class output units (see Section c). Finally, as is standard with a fully
174 connected layer, the output values (weighted scores) contributing to each output unit are summed
175 to produce a total number of points for each class. The class with the highest number of points is
176 identified as the predicted class.

177 In the original ProtoPNet, there was no location scaling. Without this location scaling, the
178 network is agnostic to *where* the input image looks most like each prototype. That is, the only
179 thing of import is that the image looks like the prototype *somewhere*. Returning to the example of
180 classifying bird images (as explored in Chen et al. (2019)), a prototype may correspond to a latent
181 representation of the red head of a red-bellied woodpecker. The original ProtoPNet does not care
182 whether a red head is found in the upper left or the upper right of the input image. Rather, the
183 ProtoPNet just considers whether a red head is present at all. For our ProtoLNet presented here,
184 the network is designed to take into consideration not only that a red head is found, but also *where*
185 within the image the red head occurs. As we will show, this consideration of location can be highly
186 beneficial in geophysical applications.

187 *b. Choosing the base CNN*

188 We envision three main approaches to choosing a base CNN. The first takes an existing CNN that
189 has been previously trained to perform classification tasks. This CNN may already be performing
190 well, but interpretability is desired. The user removes the output layer and fully connected layers of
191 their existing CNN and then use the result as their base CNN for the ProtoLNet. In this approach,
192 the ProtoLNet is used purely for interpretability of the original CNN.

193 The second approach to choosing a base CNN is to, once again, take a pre-trained CNN, remove
194 the output and fully connected layers, and then use the result as the base CNN for the ProtoLNet.
195 The difference is that now the user allows the weights within the base CNN to be further refined
196 during the ProtoLNet training in order to optimize the performance of the ProtoLNet. Allowing
197 the base CNN weights to be updated implies that the user is no longer interpreting the same base

Stage	Type	Base CNN	1x1 Layers	Prototypes	Location Scaling	Final Weights
1	train prototypes	frozen/train	train	train	train	frozen
2	replace prototypes	frozen	frozen	replace	frozen	frozen
3	train weights	frozen	frozen	frozen	frozen	train

FIG. 2. The three different stages of training the ProtoLNet.

198 CNN with which they started. However, if the goal is to create an interpretable network that is
 199 as accurate as possible, this may be a good approach. Furthermore, for image classification tasks,
 200 one might choose to use a CNN previously trained on a large dataset, e.g. VGG-19 (Simonyan and
 201 Zisserman 2014), as done by Chen et al. (2019).

202 The third approach to choosing a base CNN applies when no suitable pre-trained base CNN
 203 exists. In this case, the user must train the interpretable network from scratch. In this instance,
 204 there are two main choices. A separate base CNN could be trained, stripped of its final output and
 205 fully connected layers, and then appended to the ProtoLNet (as discussed above). Alternatively,
 206 one could initialize the base CNN with random initial weights and train it directly within the
 207 ProtoLNet architecture. We have tried both methods for the use cases explored here and found
 208 that they produced similar accuracies (although we acknowledge this may not always be the case).
 209 Here, we present results where we first pre-train a base CNN and then append it to the ProtoLNet,
 210 in order to provide a base accuracy with which to compare our ProtoLNet results.

211 *c. ProtoLNet training*

212 The training of the ProtoLNet is done in triads of stages (Fig. 2), largely following the original
 213 training approach of Chen et al. (2019). The first stage of training involves learning the prototypes
 214 by training the 1×1 layers, prototypes, location scaling grid, and the base CNN (if desired by the
 215 user; see Section b) at the same time. The final weights are frozen during this stage. The second
 216 stage of training involves replacing each prototype with the nearest latent patch within the training
 217 samples of the same class. That is, stage 1 allows the network to learn *any* form of the prototype
 218 latent patch, and stage 2 replaces this prototype with the most similar training latent patch from
 219 the same class. In this way, the prototypes always directly correspond to a latent patch in one

220 particular training sample. In the third stage of training, we freeze all elements of the ProtoLNet
221 except for the fully connected final weights (pink arrows in Fig. 1), and the network learns them
222 alone. These three stages are then cycled through multiple times (for our use cases, up to 5 times)
223 for full training of the ProtoLNet.

224 *Initialization:* Prior to stage 1, the two 1×1 convolutional layers are initialized with random
225 values drawn from a truncated normal distribution (He et al. 2015). The prototypes are initialized
226 with random values drawn from a uniform distribution between 0.0 and 1.0, and the location scaling
227 grid is initialized with ones everywhere (see Appendix B for additional details). The final weights
228 (w) that connect a prototype with its assigned class are given an initial value of 1.0, and all other
229 final weights are initialized to -0.5. The initialization of the base CNN was already discussed in
230 Section b.

231 *Stage 1:* Training is performed via stochastic gradient descent with the Adam optimizer and batch
232 size of 32. For the quadrants use case, the learning rate is set to 0.01 for every stage 1 cycle. For the
233 MJO use case, the learning rate is also initially set to 0.01 but is reduced by an order of magnitude
234 for the third cycle of stage 1 and every cycle thereafter. The network is trained with the standard
235 cross-entropy loss added to two additional loss terms: the ClusterCost and SeparationCost. The
236 cross-entropy loss penalizes the network for misclassifying the training samples. The ClusterCost
237 encourages training images to have at least one latent patch with high similarity to a prototype of
238 the same class. The SeparationCost discourages training images from having high similarity to
239 prototypes belonging to the incorrect class. Thus, the full stage 1 loss function takes the form

$$240 \quad \text{Loss} = \text{CrossEntropy} + \beta_1 \text{ClusterCost} - \beta_2 \text{SeparationCost} \quad (2)$$

241 where β_1 and β_2 are coefficients chosen by the user. Full forms of the ClusterCost and SeparationCost,
242 along with their coefficient values, are provided in Appendix C. For all use cases, we
243 train in stage 1 for 10 epochs before moving to stage 2 of training.

244 *Stage 2:* This stage does not involve any iterative training but instead is direct computation.
245 Specifically, the similarity scores are computed between each learned prototype from stage 1 and
246 every latent patch of every training image of the same class. The prototype is then *replaced* by
247 the training latent patch with the highest similarity. Note that this replacement process will nearly
248 always reduce the accuracy of the network because it replaces the stage 1-optimized prototypes

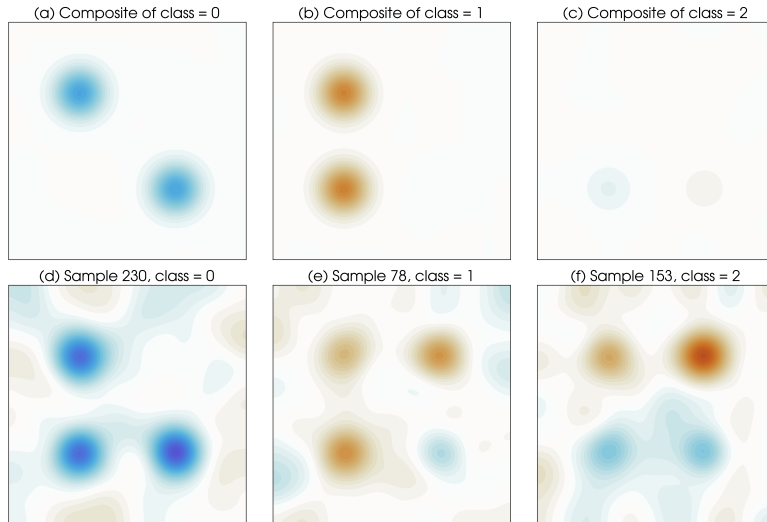
249 with something from the training set. However, this step is central to the interpretability of the
250 ProtoLNet. By cycling through all three training stages multiple times, the network learns to
251 perform well using the replaced prototypes from the training set.

252 *Stage 3:* The final weights $w_{k,j}$ connecting prototypes of class k to the output class j are learned
253 via convex optimization, since all other layers are frozen. As a reminder, all $w_{k,j}$ for $k = j$ are
254 initialized to 1.0, and the rest, $w_{k,j}$ for $k \neq j$, are initialized to -0.5. The weights are frozen for
255 stages 1 and 2 of training. In stage 3, all other free parameters in the ProtoLNet are frozen, and the
256 weights alone are trained to minimize the cross-entropy loss of the final output plus an additional
257 L_1 regularization term evaluated on the weights $w_{k,j}$ for $k \neq j$. This additional loss term provides
258 sparsity to the final model, i.e. $w_{k,j} \approx 0$ for $k \neq j$, which reduces the use of negative reasoning by
259 the network (“this does *not* look like that”). See Singh and Yow (2021) for an exploration of the
260 consequences when this sparsity requirement is relaxed. For the idealized quadrants use case, we
261 set the regularization parameter to 0.5. For the MJO use case, it is set to 0.1. For all use cases, we
262 train in stage 3 for 10 epochs. At that point, we either end training completely (i.e. we have the
263 fully trained ProtoLNet), or we cycle through stages 1-3 again.

264 3. Use Case: Idealized Quadrants

265 As a first demonstration of the ProtoLNet, we construct an idealized synthetic test set to loosely
266 represent the horizontal (latitude by longitude) spatial structures of geophysical anomalies. For
267 example, the synthetic fields (or images) could represent idealized low- and high-pressure circu-
268 lations. The anomaly fields are 100x100 pixels in size and are constructed by first initializing the
269 field with random Gaussian noise. We then randomly add an additional anomaly value (uniformly
270 distributed between 2 and 15) to the center of one or more of the four quadrants of each square
271 field. Finally, we smooth each field with a Gaussian filter with standard deviation of 7 to make
272 the fields look more like typical tropospheric pressure anomalies. Example samples are shown in
273 Fig. 3.

274 The fields in the idealized data set are assigned labels based on the sign of the anomalies in
275 each of the four quadrants of the sample (Fig. 3). Specifically, fields with negative anomalies in
276 both the second and fourth quadrants are labeled class 0, fields with positive anomalies in both the
277 second and third quadrants are labeled class 1, and all other fields are labeled class 2 (Fig. 3a-c).



274 FIG. 3. The top three panels (a-c) show composites of all samples by class label for the idealized quadrants
 275 use case. The bottom three panels (d-f) exhibit one example sample for each class.

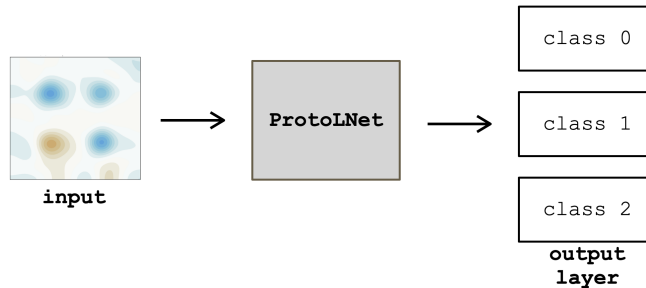


FIG. 4. Prediction setup for the idealized quadrants use case.

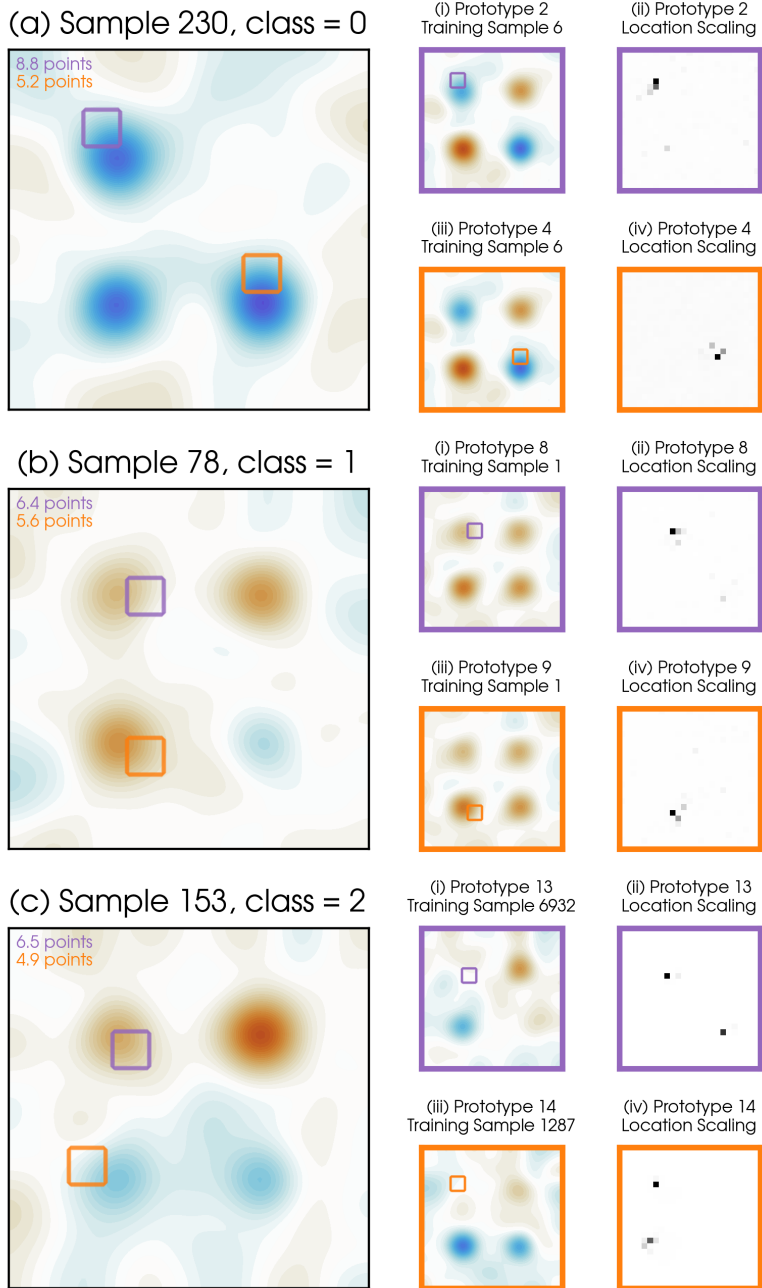
280 Fig. 3d-f show example samples for each class, demonstrating that class 0 only requires negative
 281 anomalies in the second and fourth quadrants, while any signed anomalies can exist in the other
 282 two quadrants. A similar idea exists for class 1. As will become clear, this idealized data set was
 283 designed such that the location of the different anomalies matters.

284 The synthetic data set has equally balanced classes by construction, with 3,000 samples for each
 285 of the three classes (9,000 samples total). This set is then randomly split such that 7,200 samples
 286 are used for training and 1,800 for testing. Prior to training, the input images are standardized by
 287 subtracting the mean and dividing by the standard deviation over all training pixels.

288 We task the ProtoLNet with ingesting a single input field and classifying it into one of the
289 three classes, as depicted in Fig. 4. The network cannot simply identify the existence of negative
290 anomalies (in the case of class 0) or the existence of positive anomalies (in the case of class 1).
291 Instead, it must consider the existence of different signed anomalies *and their location* within the
292 input field. To illustrate this point, we trained a ProtoPNet where location is not considered (i.e.
293 learning of the location scaling grid is turned off) and — unsurprisingly — the network fails with
294 an accuracy of 32%, no better than random chance (i.e. 33%).

295 We first train a standard CNN to perform the classification task and act as our base CNN for
296 the ProtoLNet. Details of the CNN architecture and training parameters are provided in Appendix
297 A. Once the CNN is trained, we remove the final fully connected layer and output layer, and
298 append the result to the ProtoLNet to become the base CNN (see Fig. 1). We assign 5 prototypes
299 (with $D = 128$) to each output class, for a total of 15 prototypes. Using more prototypes than
300 this yielded prototypes that rarely provided points for any sample. We cycle through the three
301 stages of ProtoLNet training (Fig. 2) five times, freezing the base CNN for the first cycle of stage
302 1 but allowing it to train for all subsequent cycles of stage 1. Once fully trained, the ProtoLNet
303 achieves an accuracy of 96%, a significant improvement over random chance and the ProtoPNet.
304 For comparison, the base CNN achieves an accuracy of 98%. The ProtoLNet is not designed to
305 outperform all alternative approaches. Instead, it is designed to provide interpretability with a
306 minimal loss in accuracy.

311 The power of the ProtoLNet is that once trained, its decision-making process can be interpreted
312 by the user. Three example predictions are shown in Fig. 5, along with their two “most winning”
313 prototypes (i.e. prototypes that gave the most points to the winning class in each example) and
314 the associated location scaling grids. To avoid any confusion, we want to clearly state that the
315 “prototypes” outlined in colored boxes in Fig. 5i,iii are not the prototypes themselves. The actual
316 prototypes are vectors of latent patches of size $1 \times 1 \times 128$ and would likely be incomprehensible
317 since they capture the output of a series of complex convolutions, poolings, and nonlinear activa-
318 tions. Instead, we visualize the group of neighboring pixels of the training field that contribute
319 to the prototype latent patch, often termed the “receptive field”. In contrast, the location scaling
320 panels in Fig. 5ii,iv display the actual grids used in the prototype layer computation, which is why



307 FIG. 5. Three example predictions by the network for the idealized quadrants use case, along with the two
 308 winning prototypes for each sample and the associated location scaling grid. For each of the three samples, there
 309 are two prototypes shown along with their associated location scaling grids. These are indexed as (i,iii) and
 310 (ii,iv), respectively.

321 the squares are much larger than the pixels in the input field (i.e. the dimensions have been reduced
322 to 25×25).

323 Consider Sample 230 (Fig. 5a), which the ProtoLNet correctly labeled as class 0. Prototypes 2
324 and 4 contributed the most points to a class 0 prediction, giving 8.8 and 5.2 points, respectively.
325 Prototype 2 was drawn from training sample 6 and, more specifically, Prototype 2 represents a
326 latent patch from the purple-boxed region of training sample 6 (Fig. 5ai). The location scaling
327 grid for Prototype 2 (Fig. 5aai) shows that this prototype is highly relevant only when found in the
328 upper-left corner of the field (dark gray and black pixels). Thus, the ProtoLNet identified high
329 similarity between Prototype 2 and an upper-left patch of Sample 230. Or in other words, the
330 ProtoLNet identified that sample 230 *looks like that* prototype *there*.

331 Prototype 4 (Fig. 5aaii,iv) also contributed points to the correct prediction of class 0. Note that
332 Prototype 4 was also drawn from training sample 6; coincidentally the same sample as Prototype
333 2. Looking at Prototypes 2 and 4 together, one can interpret that the network’s decision-making
334 strategy is to look for blue anomalies in the upper-left and bottom-right quadrants of the image
335 — which is exactly how class 0 is defined. A similar interpretation can be found for sample 78
336 (Fig. 5b) with a class label of 1. The network identifies the class 1 sample by looking for positive
337 anomalies in the upper-left and bottom-left quadrants.

338 The network’s decision-making strategy is particularly interesting for Sample 153 with a label of
339 class 2 (Fig. 5c). Prototype 13 corresponds to features associated with a weakly positive anomaly
340 in the upper-left or bottom-right quadrants. From this, it appears that the network is ruling out
341 a class 0 sample, which exhibits negative anomalies in these quadrants. Similarly, Prototype 14
342 corresponds to features associated with a weakly negative anomaly in the upper-left or bottom-left
343 quadrants. That is, the network rules out a class 1 field that exhibits strong positive anomalies in
344 these two quadrants. Fig. 5cii,iv nicely demonstrates that the location scaling grid can highlight
345 multiple locations throughout the field for the same prototype. The interpretability of the ProtoLNet
346 prediction thus allows for identification of the patches of the input field that were used to make the
347 prediction, i.e. the patches whose latent representation most looks like class-specific prototypes
348 learned during training.

349 **4. Use Case: MJO Phase Classification**

350 We next apply the ProtoLNet architecture to earth system reanalysis fields. Specifically, the net-
351 work is tasked with ingesting maps of atmospheric fields in the tropics and predicting the current
352 phase of the Madden-Julian oscillation (MJO). The MJO is a large-scale, eastward propagating cou-
353 pling between tropical wind and convection that oscillates on subseasonal (30-60 day) timescales
354 (Madden and Julian 1971, 1972; Zhang 2005). Canonical MJO events form in the Indian Ocean,
355 and propagate east into the western Pacific: the “phase” of the MJO describes roughly where it is
356 in this life cycle.

357 The task of classifying the current phase of the MJO from maps of the tropics is chosen
358 here to demonstrate the utility of our method to a relatively straightforward climate science task.
359 Classification of MJO phase requires the network to identify coherent, multivariate tropical patterns
360 on a particular (planetary) spatial scale, and the MJO’s eastward propagation also requires the
361 network to take advantage of spatial location in its decision making. Thus, while straightforward
362 from a scientific perspective, the task of classifying MJO phase is well-suited as a demonstrative
363 use-case for the ProtoLNet methodology. Toms et al. (2021) classified the state of the MJO to
364 explore the utility of explainability methods, in contrast to our interpretable method, for earth
365 system science applications.

366 We define MJO activity and phase using the “Real-time Multivariate MJO index” (RMM;
367 Wheeler and Hendon (2004)). RMM is derived through an empirical orthogonal function (EOF)
368 analysis of three variables: outgoing longwave radiation (OLR), 200 hPa zonal wind (u200) and
369 850 hPa zonal wind (u850). Each variable in RMM is pre-processed by removing the seasonal cycle
370 (i.e. the all-time mean and first three harmonics of the annual cycle on each calendar day), and the
371 previous 120-day mean of each day (to remove variability associated with longer timescales than
372 the MJO). Variables are averaged from 15N-15S, and the leading two modes of the EOF analysis
373 are used to define the MJO through two daily time series. Plotted on a 2-dimensional plane, the
374 distance of a point from the origin represents the strength of the MJO (often called the RMM
375 amplitude), and the phase angle describes the phase of the MJO, or where it is in its life cycle.
376 Following Wheeler and Hendon (2004), when the MJO is active (e.g. above a certain amplitude
377 threshold) we divide the RMM phase space into octants. Phases 1 and 2, for example, correspond

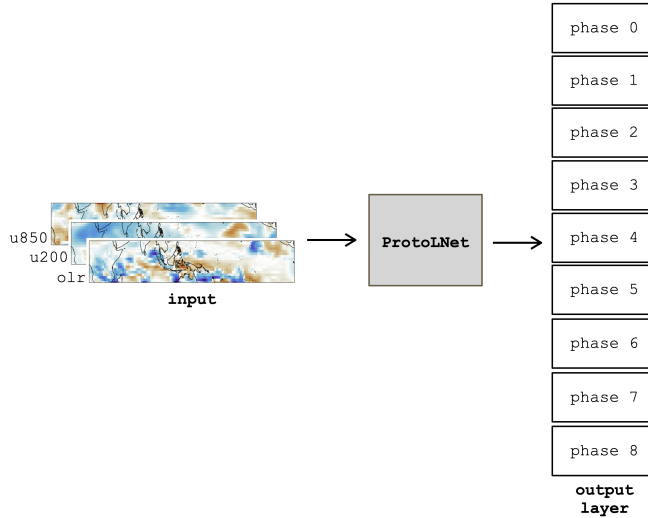


FIG. 6. Prediction setup for the MJO use case.

378 to active MJO convection in the Indian Ocean. Phases 3 and 4 are associated with activity around
 379 the Maritime Continent, etc.. If the MJO is not active, we label it as Phase 0.

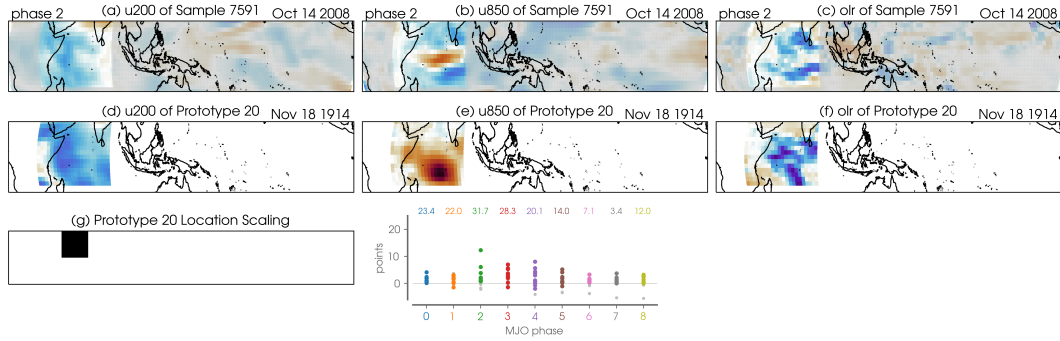
380 We define and track the MJO using ERA-20C reanalysis data (Poli et al. 2016), a reanalysis dataset
 381 than spans the entire twentieth century and provides a larger sample size than the observational
 382 record. From ERA-20C, we use daily OLR, u850, and u200 data from May 1, 1900 until December
 383 31, 2010 to calculate the RMM index. RMM is calculated from the ERA-20C data following the
 384 methodology in Wheeler and Hendon (2004) discussed above, except that the full ERA-20C period
 385 is used to define the climatology, and the processed data are projected onto the *observed* EOF
 386 modes from Wheeler and Hendon (2004) (as opposed to the EOFs from the ERA-20C data). Over
 387 the period when the observed RMM index overlaps with our ERA-20C RMM index, the two indices
 388 have a correlation of approximately 0.9 correlation, indicating very good agreement in how the
 389 RMM index is formed.

390 The network input is composed of three channels of 17 latitudes by 105 longitudes of u200,
 391 u850, and OLR, representing the three geophysical variables that go into the computation of the
 392 MJO index (see Fig. 6). Thus, a single sample has shape $17 \times 105 \times 3$. The labels are set to be the
 393 phase of the MJO, with phase 0 representing days where the amplitude of the MJO is less than 0.5.
 394 We choose to train on all available data; thus, the classes are not equally balanced across phases
 395 (see Supp. Fig. S1), although they are similar.

396 Given that there is memory of the MJO phase from one day to the next, we divide the 1900-2010
397 data into training and testing via distinct years. Specifically, the testing data is all calendar days
398 within the 22 years of 1902, 1903, 1907, 1912, 1916, 1917, 1918, 1923, 1935, 1937, 1941, 1945,
399 1946, 1949, 1953, 1961, 1965, 1976, 1992, 2007, 2008, and 2010; the training years are comprised
400 of the remaining 89 years. This results in 32,387 training samples and 8,035 testing samples.
401 The three input fields (channels) are converted to anomalies prior to analysis following a similar
402 pre-processing as for the RMM computation. That is, the time-mean calendar-day seasonal cycle is
403 subtracted from each gridpoint, and the mean of the previous 120 days is removed. Each variables
404 is individually normalized by dividing it by its tropics-wide standard deviation. Then, immediately
405 prior to training, the inputs are further standardized by the mean and standard deviation across all
406 gridpoints and channels of the training set (via flattening the input fields).

407 We first train a standard CNN to perform the classification task and act as our base CNN for the
408 ProtoLNet. Details of the CNN architecture and training parameters are provided in Appendix A.
409 Once the CNN is trained, we remove the final fully connected layer and output layer, and append
410 the result to the ProtoLNet to become the base CNN (see Fig. 1). We assign 10 prototypes (with
411 $D = 64$) to each output class, which results in a total of 90 prototypes. Fewer than 90 reduced the
412 accuracy, while using more than 90 did not improve the predictions. We cycle through the three
413 stages of ProtoLNet training (Fig. 2) five times, freezing the base CNN for the first cycle of stage
414 1, but allowing it to train on all subsequent cycles of stage 1. Once fully trained, the ProtoLNet
415 achieves a testing accuracy of 73% for classifying the phase of the MJO into one of nine classes
416 (random chance is approximately 11%), which is similar to the accuracy found in Toms et al.
417 (2021) using a black box neural network. Supp. Fig. S2 shows that the ProtoLNet exhibits testing
418 accuracies between approximately 70-80% across phases. A ProtoPNet, which does not consider
419 location, never achieves an accuracy above 30%.

420 Interestingly, the base CNN upon which our ProtoLNet was trained converged to an accuracy of
421 58%, much lower than that of the subsequent ProtoLNet. We believe that the improved accuracy
422 of the ProtoLNet may be due to the regularizing nature of the prototype architecture. That
423 is, the prototype approach constrains the network to focus on only a few latent features for phase
424 identification, allowing it to converge on an appropriate decision-making strategy when the training
425 data is limited (see discussion of additional experiments in Section 5). We believe that this may

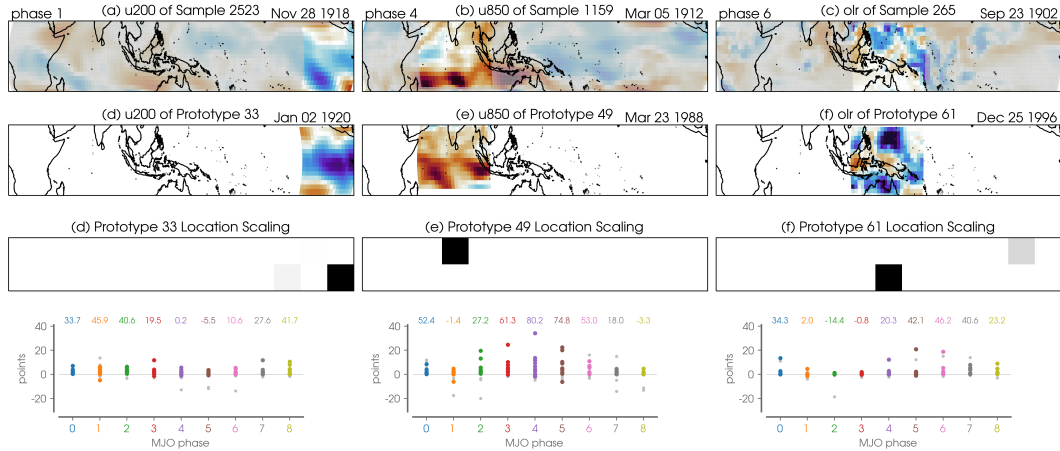


432 FIG. 7. One example prediction (testing sample 7591) by the ProtoLNet for the MJO use case, along with the
 433 winning prototype (prototype 20) and associated location scaling grid. The three columns denote the three input
 434 fields (i.e. u200, u850, olr). All anomalies are shown in panels (a)-(c) but the shading outside of the prototype
 435 patch is muted in color. The bottom middle panel show the points given to each class by each prototype, with the
 436 sum (i.e. total points) displayed along the top. Colored dots denote prototypes associated with the same class,
 437 and gray dots denote contributions from prototypes of other classes.

426 be an additional benefit of the prototype approach that is worthy of further investigation. With that
 427 said, we were able to obtain accuracies of 79% for a base CNN trained on a different training/testing
 428 split of the data. Thus, it appears the low accuracy of 58%, which we obtained consistently with
 429 other base CNNs initialized with other random seeds (not shown), is highly dependent on the
 430 training/testing split. Even so, the ProtoLNet was able to improve upon this accuracy for the
 431 specific training/testing split explored here.

438 An example of the interpretability of the ProtoLNet’s prediction for testing sample 7591 is shown
 439 in Fig. 7. This sample corresponds to phase 2 of the MJO on October 14, 2008, and the three
 440 input fields (u200, u850, and olr) are displayed across the top row for that day. All anomalies are
 441 shown, but the shading outside of the prototype receptive field is muted in color. Note that the
 442 large-scale, enhanced convection of the western Indian Ocean (Fig. 7c) is a classic indication of a
 443 phase 2 MJO event, corresponding with a coupled wind response that shows upper-level easterlies
 444 (Fig. 7a), and lower-level westerlies (Fig. 7b) in the same region.

445 The network correctly classifies this sample as phase 2, and we can use the interpretability of
 446 the ProtoLNet to further explore why. Although multiple prototypes contributed to the winning
 447 number of points for the classification of sample 7591, it can be insightful to investigate the winning

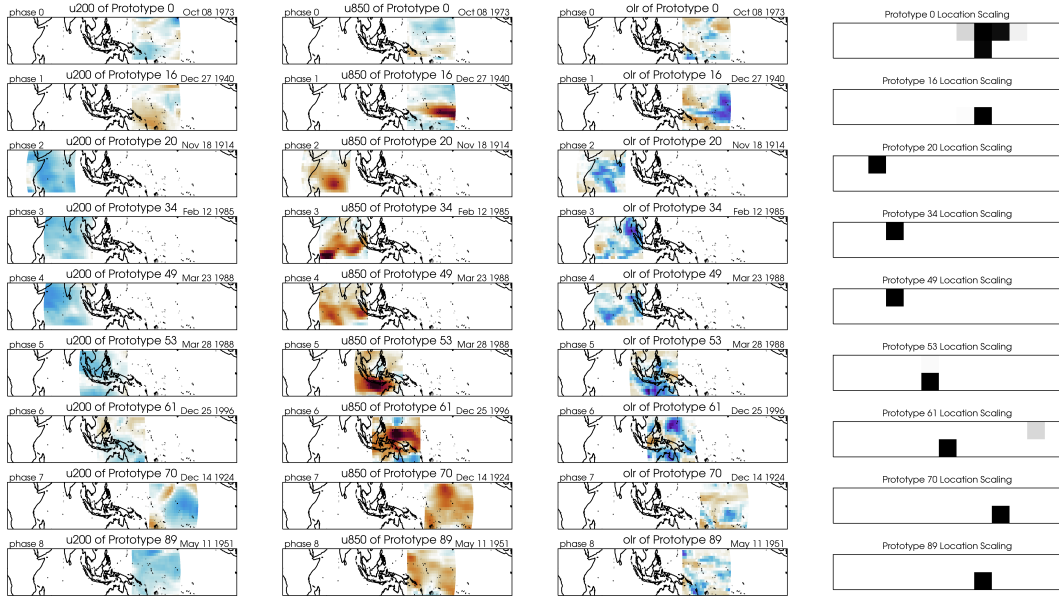


457 FIG. 8. As in Fig. 7, but for three additional example testing samples (one per column) displaying only one
 458 geophysical field for each.

448 prototype (i.e. the prototype that contributes the most points). With multiple channels as input,
 449 the winning prototype for this sample (Prototype #20) is visualized as three different fields, one
 450 for each input variable (i.e. u200, u850, olr), as shown in Fig. 7d-f. Prototype 20 is a latent
 451 patch corresponding to the state of the western Indian Ocean on November 18, 1914. The location
 452 scaling grid associated with Prototype 20 (Fig. 7g) highlights that similarities to this prototype are
 453 only heavily weighted when found at these longitudes. Thus, we see that the anomaly fields on
 454 October 14, 2008, for sample 7591 look a lot like those of Prototype 20, with upper-level easterlies,
 455 lower-level westerlies and enhanced convection over the western Indian Ocean. This provides
 456 evidence for why the network classified this sample as MJO phase 2.

459 Fig. 8 shows three additional (correctly predicted) testing samples and their winning prototypes,
 460 displaying only one geophysical field for each prediction to simplify the figure. Sample 2523 on
 461 November 28, 1918, is classified as phase 1, in part because its upper-level easterlies *look like*
 462 those of Prototype 33 from January 2, 1920 over the eastern Pacific (Fig. 8a,d). The lower-level
 463 westerlies over the Indian Ocean on March 5, 1912, *look like* those of phase 4 Prototype 49 from
 464 March 23, 1988 (Fig. 8b,e). Enhanced convection as seen by the OLR field east of the Maritime
 465 Continent on September 23, 1902 *looks like* that of phase 6 Prototype 61 (Fig. 8c,f).

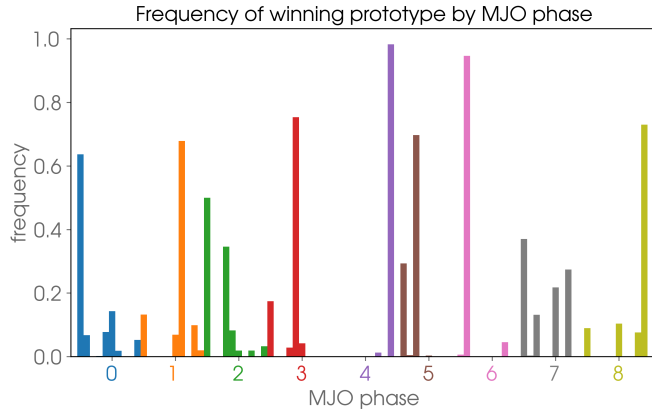
468 As a summary of the MJO classification results, Fig. 9 displays the most frequently winning
 469 prototype for each phase of the MJO. A hallmark feature of the MJO is its eastward propagation,



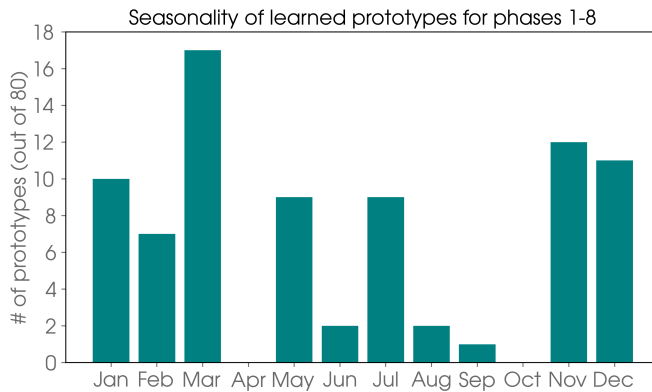
466 FIG. 9. The most frequently winning prototype for correctly classified testing samples by MJO phase. Each
 467 column represents a different input variable; the fourth column displays the associated location scaling.

470 and Fig. 9 reveals the eastward progression of the prototypes (and associated location scaling
 471 grids) starting in phase 2 and continuing to phases 7 and 8. That is, the ProtoLNet, with its
 472 location-specific focus, has learned representative prototypes that move eastward with the known
 473 progression of the MJO. Phase 1, however, does not appear to behave this way. Prototype 16 is
 474 often the most-winning prototype for phase 1, but it is focused over the mid-Pacific rather than
 475 the western Indian Ocean as one might expect (this is true for most of the Phase 1 prototypes; see
 476 Supp. Fig. S5). The reason why phase 1 prototypes tend to focus on this region is not clear, but we
 477 hypothesize the network may be focusing on wind signals in this region associated with a phase 1
 478 event forming or a previous MJO event decaying. Further investigation is needed.

482 Fig. 10 shows a breakdown of how often (i.e. for how many testing samples) each prototype
 483 was the winning prototype. For example, Prototype 49 from March 23, 1988, is the most-winning
 484 prototype for phase 4, and it is the winning prototype for 98% of all correctly classified phase 4
 485 testing samples. This suggests that this prototype is highly indicative of phase 4 MJO events. On
 486 the other hand, phase 7 has multiple prototypes that frequently earn the title of winning prototype.



479 FIG. 10. The frequency that each prototype is the winning prototype (i.e. contributes the most points to the
 480 predicted class) for each correctly classified testing sample. Each phase has 10 possible prototypes; however,
 481 there are some prototypes that are never a winning prototype. They have frequency of zero.



489 FIG. 11. Number of learned prototypes for MJO phases 1-8 (excluding phase 0, so out of 80 prototypes total)
 490 binned by month of the year of the training sample from which the prototype was drawn.

487 Thus, Prototype 70 (displayed in Fig. 9) should be interpreted as only one possible indicator of
 488 phase 7.

491 All 10 learned prototypes for each phase are provided in the Supp. Fig. S4-S12. Fig. 11 shows the
 492 breakdown of the monthly distribution for all prototypes for active MJO phases 1-8. The network
 493 preferentially chooses prototypes from November-March when the MJO is known to be most active,
 494 however, prototypes from May and July are also learned, likely to capture the differences in MJO

495 behavior across seasons (Zhang 2005). The monthly seasonality for all prototypes, including those
496 for MJO phase 0, are shown in Supp. Fig. S3.

497 **5. Discussion**

498 The value of the ProtoLNet design is that interpretation of the network’s decision-making process
499 is baked into the architecture itself, rather than performed *post-hoc* like most explainable AI methods
500 (Buhrmester et al. 2019; Barredo Arrieta et al. 2020; Samek et al. 2021). Although the network
501 is constrained to only learn via similarities to a small number of learned prototypes, multiple use
502 cases demonstrate that it can be trained to exhibit only a small reduction in accuracy compared to
503 non-interpretable architectures (Chen et al. 2019; Singh and Yow 2021). Moreover, for our MJO
504 use case, the ProtoLNet actually improved in accuracy over its base CNN. We hypothesize that this
505 is because the ProtoLNet greatly reduces the search space possibilities, which allows the network
506 to converge on a good prediction strategy given a limited sample size. One might think of this as
507 a form of regularization, or instead, a form of physics-guided constraint (e.g. Beucler et al. 2021)
508 that forces the network to learn physically realizable evidence for each class. To further explore this
509 hypothesis, we trained additional ProtoLNets for the idealized quadrants use case (Section 3), but
510 with a much smaller training size (only 1,400 samples for training). In all cases, the ProtoLNets
511 obtained higher testing accuracies — sometimes significantly higher — than their respective base
512 CNNs (see results in Supp. Fig. S13). This is not to say that the ProtoLNet is categorically more
513 accurate than a standard CNN. A more thorough exploration of the hyperparameter space could
514 bring the base CNN accuracy up to that of the ProtoLNet. Instead, we just wish to highlight that
515 with minimal tuning, the ProtoLNet was able to consistently achieve high accuracies with limited
516 training data.

517 In addition to being interpretable, the ProtoLNet provides the benefit of learning a small subset
518 of prototypical parts *from the training set* that reflect identifiable features for each output class.
519 That is, each prototype is found “in the wild” and, thus, has a direct connection to a sample that
520 has occurred. This should be distinguished from more standard architectures that learn complex
521 latent representations and features that may never occur in reality. For the case of MJO phase
522 classification, this means that the network can learn particular example MJO events that generalize
523 across the observational record and reflect identifiable features for each specific MJO phase.

524 Thus, although predicting the current phase of the MJO is routine from a scientific perspective,
525 the ProtoLNet allows us to look back and identify specific dates that exhibit prototypical MJO
526 phase behaviour, as shown in Fig. 9 and Fig. 11. Furthermore, it is straightforward to extend the
527 interpretable ProtoLNet setup of Fig. 6 to ingest current atmospheric fields and predict the MJO
528 phase at some lead time into the future.

529 As we have used it here, the ProtoLNet design learns localized prototypes from the input that
530 provide evidence for a particular output class. This should be distinguished from the standard
531 climate approach that composites the input fields over many samples for a single class, and thus
532 results in a smooth averaged field (assuming there are enough samples to average out the noise).
533 Such a composite field is computed pixel by pixel and as such, does not capture shared gradients or
534 higher-level features that can be learned by the convolutional layers of the ProtoLNet. Finally, as
535 discussed above, the ProtoLNet identifies prototypical behavior that has been realized in a training
536 sample, while the composite field provides a smoothed, idealized picture that will likely never be
537 observed.

538 The ProtoLNet is based on the ProtoPNet of Chen et al. (2019) which uses positive reasoning,
539 i.e. *this looks like that*, to predict the correct class of an input image. Singh and Yow (2021)
540 introduce a variation, the NP-ProtoPNet, which additionally includes negative reasoning, i.e. *this*
541 *does not look like that*. Their argument is that by allowing negative reasoning, the network is able
542 to better rule out incorrect classes and achieve accuracies on-par with the best performing black box
543 models. It is straightforward to apply our location-scaling grid to a NP-ProtoPNet, which mainly
544 involves relaxing the sparsity requirement of the final weights layer. However, by allowing both
545 positive and negative reasoning, interpreting the model’s decision making process may become
546 significantly more difficult due to competing negative and positive point contributions to the final
547 output classes. Thus, we chose to focus on positive reasoning for this study.

548 **6. Conclusions**

549 Driven by the desire to explain the decision-making process of deep learning models, a large
550 variety of *post hoc* explainability methods have been developed (e.g. Buhrmester et al. 2019;
551 Barredo Arrieta et al. 2020; Samek et al. 2021). However, these explainability methods come with
552 their own challenges (Kindermans et al. 2019; Mamalakis et al. 2021) and recent work by Rudin

553 (2019) and Chen et al. (2019) suggest that instead of trying to explain black box models, we should
554 be creating models where the decision-making process is interpretable by design.

555 Here, we extend the interpretable ProtoPNet of Chen et al. (2019) to consider absolute location
556 in the interpretable prototype architecture, which we term the ProtoLNet. The results of our
557 work can be summarized by three main conclusions. (1) Considering absolute location in the
558 ProtoLNet architecture greatly improves accuracy for the geophysical use cases explored here. (2)
559 The ProtoLNet is interpretable in that it directly provides which prototypes are similar to different
560 patches of an input image (i.e. *this looks like that*), and where these prototypes matter (i.e. *there*).
561 (3) The network is able to learn specific historical dates that serve as multivariate prototypes of the
562 different Madden-Julian oscillation phases.

563 This work serves as one example of an interpretable deep learning model specifically designed
564 for earth system science applications (see also Sonnewald and Lguensat 2021). There is much
565 more research to be done on the topic. For example, the incorporation of negative reasoning
566 and extension to regression tasks could be beneficial for its use in earth science. Furthermore,
567 the interpretation and utility of the learned prototypes themselves, apart from the prediction task,
568 leaves much to be explored. Thus, this work should be seen as merely a step in the direction of
569 interpretable deep learning for earth science exploration.

570 *Acknowledgments.* This work was funded, in part, by the NSF AI Institute for Research on
571 Trustworthy AI in Weather, Climate, and Coastal Oceanography (AI2ES) under NSF grant ICER-
572 2019758. ZKM recognizes support from the National Science Foundation under Award No.
573 2020305. JKR recognizes support from the U.S. Department of Energy, Office of Science, Office of
574 Advanced Scientific Computing Research, Department of Energy Computational Science Graduate
575 Fellowship under Award No. DE-SC0020347.

576 *Data availability statement.* Once published, the code will be made available to the community
577 via a permanent DOI on Zenodo. For peer-review, the code is available at [https://github.com/
578 eabarnes1010/tlltt](https://github.com/eabarnes1010/tlltt). The ERA-20C is publically available at [https://www.ecmwf.int/en/
579 forecasts/datasets/reanalysis-datasets/era-20c](https://www.ecmwf.int/en/forecasts/datasets/reanalysis-datasets/era-20c).

580 APPENDIX A

581 **Base CNN architectures and training**

582 The base CNN for the idealized quadrants use case (Section 3) has two convolutional layers of 32
583 kernels each. Every convolutional layer is followed by an average pooling layer with kernel size
584 2×2 and a stride length of 2. The output of the final average pooling layer is flattened, and then
585 fed into a final dense layer of 64 units which is fed into the final output layer of 3 units. The final
586 output layer contains the softmax activation function which convert the outputs into confidences
587 that sum to 1.0. The final dense layer is trained with dropout (Srivastava et al. 2014) at a rate of
588 0.4 to reduce overfitting. When the base CNN is appended to the ProtoLNet, the dropout rate is
589 set to zero. That is, dropout is only used to reduce overfitting during the pre-training of the base
590 CNN. The base CNN is trained with a fixed learning rate of $5e-5$ for 12 epochs.

591 The base CNN for the MJO use case (Section 4) has three convolutional layers of 16 kernels
592 each. Every convolutional layer is followed by an average pooling layer with kernel size 2×2 and
593 a stride length of 2. The convolutional layers are trained with dropout at a rate of 0.4 to reduce
594 overfitting. The output of the final average pooling layer is flattened, and then fed into a final dense
595 layer of 32 units that is fed into the final output layer of 9 units. The final output layer contains
596 the softmax activation function which converts the outputs into confidences that sum to 1.0. The
597 final dense layer is trained with dropout at a rate of 0.2. When the base CNN is appended to the
598 ProtoLNet, the dropout rates are set to zero. That is, dropout is only used to reduce overfitting

599 during the pre-training of the base CNN. The base CNN is trained with a fixed learning rate of
 600 0.00017548 for 23 epochs.

601 APPENDIX B

602 Learning location scaling exponents

603 The location scaling values must be non-negative. Subsequently, we use a trick from Duerr et al.
 604 (2020) and learn the exponents of the location scaling, rather than the values themselves. That is,
 605 if s_k denotes the location scaling value for prototype \mathbf{p} at latent patch k then

$$606 \quad s_k = e^{\gamma_k}, \quad (\text{B1})$$

607 where the free parameter γ_k is *learned* by the network during training. Thus, at initialization, all
 608 γ_k values are initialized to zero so that the location scaling grid (all s_k values) is initialized to a
 609 grid of ones.

610 APPENDIX C

611 Stage 1 loss function

612 The Stage 1 loss function is given by Equation 2. There are three components: the usual CrossEn-
 613 tropy, plus a ClusterCost, and minus a SeparationCost.

614 Consider a set of input samples and associated class labels $\{(\mathbf{x}_i, y_i) : i = 1, 2, \dots, N\}$. The output
 615 from the extended CNN given sample \mathbf{x}_i is a quilt of latent patches \mathbf{z}_{ik} , where k indexes the latent
 616 patches. For the architecture shown in Figure 1, $k \in \{1, 2, \dots, 6\}$ because the quilt is 2×3 . Let s_k
 617 denote the current location scaling value associated with latent patch k , and \mathbf{P}_{y_i} denote the set of
 618 all prototypes belonging to class y_i . The ClusterCost is given by

$$619 \quad \text{ClusterCost} = \frac{1}{N} \sum_{i=1}^N \left[\min_{\mathbf{p} \in \mathbf{P}_{y_i}} \min_k \frac{\|\mathbf{z}_{ik} - \mathbf{p}\|_2^2}{s_k + \epsilon} \right] \quad (\text{C1})$$

620 where $\|\cdot\|_2^2$ is the squared L_2 norm and ϵ is a small number, there to guard against divide-by-zero
 621 problems.

622 The ClusterCost encourages training images to have at least one latent patch with high similarity
623 to a prototype of the same class. The computation is based on Chen et al. (2019), but incorporates
624 the location scaling grid introduced in this paper.

625 The SeparationCost discourages training images from having high similarity to prototypes be-
626 longing to the incorrect class. The computation is almost identical to that of the ClusterCost. The
627 difference is that we minimize over the set of all prototypes that do not belong to class y_i .

$$628 \text{SeparationCost} = \frac{1}{N} \sum_{i=1}^N \left[\min_{\mathbf{p} \notin \mathbf{P}_{y_i}} \min_k \frac{\|\mathbf{z}_{ik} - \mathbf{p}\|_2^2}{s_k + \epsilon} \right] \quad (\text{C2})$$

629 For the idealized quadrants use case, we set the ClusterCost coefficient $\beta_1 \approx 0.17$ (see code for
630 all digits) and the SeparationCost coefficient $\beta_2 = \beta_1/10$. For the MJO use case $\beta_1 = 0.2$ and
631 $\beta_2 = \beta_1/10$. Note the negative sign in front of the SeparationCost term in Equation 2 encourages
632 the network to have larger separation (lower similarity) between samples and the prototypes from
633 incorrect classes.

634 References

635 Balmaseda, M., and Coauthors, 2020: NOAA-DOE precipitation processes and predictability
636 workshop. Tech. Rep. DOE/SC-0203; NOAA Technical Report OAR CPO-9., U.S. Department
637 of Energy and U.S. Department of Commerce NOAA.

638 Barnes, E. A., B. Toms, J. W. Hurrell, I. Ebert-Uphoff, C. Anderson, and D. Anderson, 2020: Indi-
639 cator Patterns of Forced Change Learned by an Artificial Neural Network. *Journal of Advances in*
640 *Modeling Earth Systems*, **n/a (n/a)**, e2020MS002 195, <https://doi.org/10.1029/2020MS002195>.

641 Barredo Arrieta, A., and Coauthors, 2020: Explainable artificial intelligence (XAI): Concepts,
642 taxonomies, opportunities and challenges toward responsible AI. *Inf. Fusion*, **58**, 82–115,
643 <https://doi.org/10.1016/j.inffus.2019.12.012>.

644 Beucler, T., M. Pritchard, S. Rasp, J. Ott, P. Baldi, and P. Gentine, 2021: Enforcing analytic
645 constraints in neural networks emulating physical systems. *Phys. Rev. Lett.*, **126 (9)**, 098 302,
646 <https://doi.org/10.1103/PhysRevLett.126.098302>.

- 647 Buhrmester, V., D. Münch, and M. Arens, 2019: Analysis of explainers of black box deep neural
648 networks for computer vision: A survey. *arXiv*, 1911.12116.
- 649 Chen, C., O. Li, D. Tao, A. Barnett, C. Rudin, and J. K. Su, 2019: This looks like that: Deep learning
650 for interpretable image recognition. *Advances in Neural Information Processing Systems*, Curran
651 Associates, Inc., Vol. 32.
- 652 Davenport, F. V., and N. S. Diffenbaugh, 2021: Using machine learning to analyze physical causes
653 of climate change: A case study of U.S. midwest extreme precipitation. *Geophys. Res. Lett.*,
654 <https://doi.org/10.1029/2021gl093787>.
- 655 Duerr, O., B. Sick, and E. Murina, 2020: *Probabilistic Deep Learning: With Python, Keras and*
656 *Tensorflow Probability*. MANNING PUBN.
- 657 He, K., X. Zhang, S. Ren, and J. Sun, 2015: Delving deep into rectifiers: Surpassing Human-Level
658 performance on ImageNet classification. *2015 IEEE International Conference on Computer*
659 *Vision (ICCV)*, 1026–1034, <https://doi.org/10.1109/ICCV.2015.123>.
- 660 Irrgang, C., N. Boers, M. Sonnewald, E. A. Barnes, C. Kadow, J. Staneva, and J. Saynisch-
661 Wagner, 2021: Towards neural earth system modelling by integrating artificial intelligence in
662 earth system science. *Nature Machine Intelligence*, **3 (8)**, 667–674, <https://doi.org/10.1038/s42256-021-00374-3>.
- 664 Keys, P. W., E. A. Barnes, and N. H. Carter, 2021: A machine-learning approach to human
665 footprint index estimation with applications to sustainable development. *Environ. Res. Lett.*,
666 **16 (4)**, 044 061, <https://doi.org/10.1088/1748-9326/abe00a>.
- 667 Kindermans, P.-J., S. Hooker, J. Adebayo, M. Alber, K. T. Schütt, S. Dähne, D. Erhan, and
668 B. Kim, 2019: The (un)reliability of saliency methods. *Explainable AI: Interpreting, Explaining*
669 *and Visualizing Deep Learning*, W. Samek, G. Montavon, A. Vedaldi, L. K. Hansen, and K.-
670 R. Müller, Eds., Springer International Publishing, Cham, 267–280, https://doi.org/10.1007/978-3-030-28954-6_14.
- 672 Lapuschkin, S., S. Wäldchen, A. Binder, G. Montavon, W. Samek, and K.-R. Müller, 2019:
673 Unmasking clever hans predictors and assessing what machines really learn. *Nat. Commun.*,
674 **10 (1)**, 1096, <https://doi.org/10.1038/s41467-019-08987-4>.

675 Madden, R. A., and P. R. Julian, 1971: Detection of a 40-50 day oscillation in the zonal wind
676 in the tropical pacific. *Journal of Atmospheric Sciences*, **28 (5)**, 702 – 708, [https://doi.org/](https://doi.org/10.1175/1520-0469(1971)028<0702:DOADOI>2.0.CO;2)
677 10.1175/1520-0469(1971)028<0702:DOADOI>2.0.CO;2, URL [https://journals.ametsoc.org/](https://journals.ametsoc.org/view/journals/atsc/28/5/1520-0469_1971_028_0702_doadoi_2_0_co_2.xml)
678 view/journals/atsc/28/5/1520-0469_1971_028_0702_doadoi_2_0_co_2.xml.

679 Madden, R. A., and P. R. Julian, 1972: Description of global-scale circulation cells in the tropics
680 with a 40-50 day period. *Journal of Atmospheric Sciences*, **29 (6)**, 1109 – 1123, [https://doi.org/](https://doi.org/10.1175/1520-0469(1972)029<1109:DOGSCC>2.0.CO;2)
681 10.1175/1520-0469(1972)029<1109:DOGSCC>2.0.CO;2, URL [https://journals.ametsoc.org/](https://journals.ametsoc.org/view/journals/atsc/29/6/1520-0469_1972_029_1109_dogscc_2_0_co_2.xml)
682 view/journals/atsc/29/6/1520-0469_1972_029_1109_dogscc_2_0_co_2.xml.

683 Mamalakis, A., I. Ebert-Uphoff, and E. A. Barnes, 2021: Neural Network Attribution Methods
684 for Problems in Geoscience: A Novel Synthetic Benchmark Dataset. *arXiv*, 2103.10005, 2103.
685 10005.

686 McGovern, A., R. Lagerquist, D. John Gagne, G. E. Jergensen, K. L. Elmore, C. R. Homeyer,
687 and T. Smith, 2019: Making the black box more transparent: Understanding the physical
688 implications of machine learning. *Bull. Am. Meteorol. Soc.*, **100 (11)**, 2175–2199, [https://doi.org/](https://doi.org/10.1175/BAMS-D-18-0195.1)
689 10.1175/BAMS-D-18-0195.1.

690 Montavon, G., W. Samek, and K.-R. Müller, 2018: Methods for interpreting and understanding deep
691 neural networks. *Digit. Signal Process.*, **73**, 1–15, <https://doi.org/10.1016/j.dsp.2017.10.011>.

692 National Academies of Sciences Engineering and Medicine, 2020: *Earth System Predictability*
693 *Research and Development: Proceedings of a Workshop-in Brief*. The National Academies
694 Press, Washington, DC, <https://doi.org/10.17226/25861>.

695 Philander, S. G. H., 1983: El niño southern oscillation phenomena. *Nature*, **302 (5906)**, 295–301,
696 <https://doi.org/10.1038/302295a0>.

697 Poli, P., and Coauthors, 2016: Era-20c: An atmospheric reanalysis of the twentieth century.
698 *Journal of Climate*, **29 (11)**, 4083 – 4097, <https://doi.org/10.1175/JCLI-D-15-0556.1>, URL
699 <https://journals.ametsoc.org/view/journals/clim/29/11/jcli-d-15-0556.1.xml>.

700 Rasp, S., H. Schulz, S. Bony, and B. Stevens, 2019: Combining crowd-sourcing and deep learning
701 to understand meso-scale organization of shallow convection. *arXiv*, 1906.01906.

702 Rudin, C., 2019: Stop explaining black box machine learning models for high stakes decisions and
703 use interpretable models instead. *Nature Machine Intelligence*, **1** (5), 206–215, [https://doi.org/](https://doi.org/10.1038/s42256-019-0048-x)
704 10.1038/s42256-019-0048-x.

705 Samek, W., G. Montavon, S. Lapuschkin, C. J. Anders, and K.-R. Müller, 2021: Explaining
706 deep neural networks and beyond: A review of methods and applications. *Proc. IEEE*, **109** (3),
707 247–278, <https://doi.org/10.1109/JPROC.2021.3060483>.

708 Simonyan, K., and A. Zisserman, 2014: Very deep convolutional networks for Large-Scale image
709 recognition. *arXiv*, 1409.1556.

710 Singh, G., and K.-C. Yow, 2021: These do not look like those: An interpretable deep learning
711 model for image recognition. *IEEE Access*, **9**, 41 482–41 493, [https://doi.org/10.1109/ACCESS.](https://doi.org/10.1109/ACCESS.2021.3064838)
712 2021.3064838.

713 Sonnewald, M., and R. Lguensat, 2021: Revealing the impact of global heating on north atlantic
714 circulation using transparent machine learning. *J. Adv. Model. Earth Syst.*, **13** (8), [https://doi.org/](https://doi.org/10.1029/2021ms002496)
715 10.1029/2021ms002496.

716 Srivastava, N., G. Hinton, A. Krizhevsky, I. Sutskever, and R. Salakhutdinov, 2014: Dropout: a
717 simple way to prevent neural networks from overfitting. *J. Mach. Learn. Res.*, **15** (1), 1929–1958.

718 Toms, B. A., E. A. Barnes, and I. Ebert-Årnhoff, 2020: Physically Interpretable Neural Networks
719 for the Geosciences: Applications to Earth System Variability. *Journal of Advances in Modeling*
720 *Earth Systems*, <https://doi.org/10.1029/2019MS002002>.

721 Toms, B. A., K. Kashinath, D. Yang, and Prabhat, 2021: Testing the reliability of interpretable
722 neural networks in geoscience using the Madden–Julian oscillation. *Geosci. Model Dev.*, **14** (7),
723 4495–4508, <https://doi.org/10.5194/gmd-14-4495-2021>.

724 Wheeler, M. C., and H. H. Hendon, 2004: An all-season real-time multivariate mjo in-
725 dex: Development of an index for monitoring and prediction. *Monthly Weather Review*,
726 **132** (8), 1917 – 1932, [https://doi.org/10.1175/1520-0493\(2004\)132<1917:AARMMI>2.0.CO;](https://doi.org/10.1175/1520-0493(2004)132<1917:AARMMI>2.0.CO;2)
727 2, URL [https://journals.ametsoc.org/view/journals/mwre/132/8/1520-0493_2004_132_1917_](https://journals.ametsoc.org/view/journals/mwre/132/8/1520-0493_2004_132_1917_aarmmi_2.0.co_2.xml)
728 [aarmmi_2.0.co_2.xml](https://journals.ametsoc.org/view/journals/mwre/132/8/1520-0493_2004_132_1917_aarmmi_2.0.co_2.xml).

729 Zhang, C., 2005: Madden-Julian oscillation. *Reviews of Geophysics*, **43** (2),
730 <https://doi.org/https://doi.org/10.1029/2004RG000158>, URL <https://agupubs.onlinelibrary.wiley.com/doi/abs/10.1029/2004RG000158>,
731 <https://agupubs.onlinelibrary.wiley.com/doi/pdf/10.1029/2004RG000158>,
732 <https://agupubs.onlinelibrary.wiley.com/doi/pdf/10.1029/2004RG000158>.